ADVANCED FUNCTIONAL MATERIALS
www.afm-journal.de

Stretchable Electronic Facial Masks for Skin Electroporation

*Xinkai Xu, Liang Guo, Hao Liu, Zanxin Zhou, Shuang Li, Qi Gu, Shenglong Ding, Haitao Guo, Yan Yan, Yuqun Lan, Qinlan Li, Wanxin Wei, Jian Zhang, Chong Liu, and Yewang Su**

A stretchable electronic facial mask (SEFM) for skin electroporation by transdermal drug delivery is introduced. The SEFM exhibits characteristics of reusability, water-resistant, low cost, and portability. To achieve these objectives while maintaining satisfactory mechanical and electrical performance of the device, two main areas are innovated: (1) Grinding and doping modification of conductive ink to enhance its adhesion to silicone and increase conductivity through material research, as well as mechanical structure design for stretching stability of conductive ink electrodes. (2) Doping modification of high-temperature vulcanizes silicone to address the issue of increased resistance during encapsulation due to the swell of conductive ink. The SEFM designed with these innovations, is validated in rat experiments, demonstrating a 3–4 times increase in drug intake compared to the control group without skin electroporation. Safety is confirmed, and the promotion of niacinamide drug delivery is verified in human volunteers. The materials-modified conductive ink and conductive silicone proposed in SEFM can be employed in other flexible wearable devices, and this platform has the potential for future integration of additional components to achieve expanded functionality and productization.

1. Introduction

Facial dermatosis affects a significant number of individuals worldwide, with acne alone impacting 9.4% of the global population.[1] According to statistics, patients with facial dermatosis not merely experience pain, itching, or numbness, but also commonly face anxiety and depression, which may lead to severe social avoidance and communication barriers, and even suicidal ideation.[2] Therefore, treating relevant skin conditions with medication or improving skin health through the delivery of nutrients is of significant importance. Facial dermatosis is often a chronic condition that requires long-term drug therapy and improvement in skin condition. Transdermal drug delivery is an effective method in this regard. Compared to oral and injectable administration, transdermal delivery avoids gastrointestinal absorption and metabolism, as well

X. Xu, L. Guo, H. Liu, Z. Zhou, S. Li, Y. Lan, Q. Li, Y. Su
State Key Laboratory of Nonlinear Mechanics
Institute of Mechanics
Chinese Academy of Sciences
Beijing 100190, China
E-mail: yewangsu@imech.ac.cn

X. Xu, Z. Zhou, S. Li, Y. Lan, Q. Li, J. Zhang, C. Liu, Y. Su
School of Engineering Science
University of Chinese Academy of Sciences
Beijing 100049, China

L. Guo, H. Liu
Zhongke Carrying Equipment Technology Co.
Beijing 101407, China

Q. Gu, S. Ding, H. Guo
State Key Laboratory of Membrane Biology
Institute of Zoology
Chinese Academy of Sciences
Chaoyang District, Beijing 100101, China

Q. Gu
Beijing Institute for Stem Cell and Regenerative Medicine
Chaoyang District, Beijing 100101, China

Q. Gu
University of Chinese Academy of Sciences
Huairou District, Beijing 101449, China

S. Ding
Department of Foot and Ankle Surgery
Beijing Tongren Hospital
Capital Medical University
Beijing 100730, China

Y. Yan
Cosmetic Technology Center
Chinese Academy of Inspection and Quarantine
Beijing 100176, China

W. Wei
State Key Laboratory of Solid Lubrication
Lanzhou Institute of Chemical Physics
Chinese Academy of Sciences
Lanzhou 730000, China

J. Zhang
Key Laboratory for Mechanics in Fluid Solid Coupling Systems
Institute of Mechanics
Chinese Academy of Sciences
Beijing 100190, China

C. Liu
State Key Laboratory of High Temperature Gas Dynamics
Institute of Mechanics
Chinese Academy of Sciences
Beijing 100190, China

The ORCID identification number(s) for the author(s) of this article can be found under https://doi.org/10.1002/adfm.202311144

DOI: 10.1002/adfm.202311144

as reduces pain, thereby improving patient compliance.[3,4] However, due to the presence of the skin barrier, only a small fraction of drugs can passively diffuse through the skin, and the rate is often slow, making it challenging to maintain an effective drug delivery level.[5] Researchers have developed various methods to enhance drug penetration into the skin. Among these methods, electroporation involves application of high-voltage pulses, which significantly improves drug penetration efficiency.[6] In comparison to other methods such as chemical enhancers,[7–9] electrophoresis,[10–13] sonophoresis,[5,14–16] and microneedles,[17–19] electroporation respectively offers advantages in terms of facilitating the delivery of large drug molecules, noncorrosiveness at the electrode site, low equipment fabrication costs, and noninvasiveness.[4,20]

Designing and fabricating a wearable, flexible transdermal drug delivery device for skin electroporation, holds great appeal and significant application value for individuals of all ages, who require treatment for dermatological conditions. The challenges and optimizations associated with fabricating devices at a mature product stage, rather than at a prototype level, encompass the following: 1) Skin close fit. Skin electroporation requires the delivery of voltage through electrodes to the surface of the skin, necessitating a close fit between the electrodes and the facial skin to ensure optimal electrical connection. 2) Hands-free operation for prolonged personal use. Transdermal drug therapy typically involves treatment durations over 10 min, during which it is preferable for the hands to be free to perform other tasks. 3) Adaptability to large-area complex surfaces. The human face is a complex surface characterized by a large area and intricate curvature, with multiple depressions and protrusions corresponding to regions like the eyes, nose, mouth, etc. Compared to the skin on the back, abdomen, and legs of the body, facial skin exhibits relatively complex features (Note S1 and Figure S1, Supporting Information), and skin electroporation devices require a close fit with such a surface. 4) Device reusability and robustness. Given the prolonged treatment duration of transdermal drug delivery, skin electroporation devices designed to facilitate drug penetration need to be reusable and exhibit high reliability. 5) Portability. Skin electroporation devices need to ensure their portability so that they can be used during travel or other activities. 6) Low cost. The significant prevalence of facial dermatosis requires cost-effective skin electroporation devices, ensuring affordability for the large population in need of treatment. The current desktop and handheld skin electroporation devices are not capable of hands-free operation and have difficulties in conforming to the entire facial area.[21,22] Additionally, the flexible delivery device enables extensive skin coverage and offers portability,[23] but it is expensive to produce and involves complex manufacturing processes, hindering mass production.

In this paper, we introduce a stretchable electronic facial mask (SEFM) for skin electroporation, which addresses the six aforementioned challenges and exhibits characteristics such as reusability, water-resistant, low cost, and portability. We primarily innovated in two key areas. First, we conducted grinding and doping modification of conductive ink to enhance its adhesion to silicone by incorporating silicone oil, and to increase the conductivity of conductive ink electrodes by adding graphene. We also ensured stretching stability of the conductive ink electrodes through mechanical structure design. Second, we doped-modified high-temperature vulcanized silicone with carbon black to address the problem of increased overall resistance during encapsulation due to the swell of conductive ink. These design principles can be extended to the fabrication of other stretchable electronic devices. Finally, we experimentally validated SEFM through animal experiments, confirming its efficacy in accelerating the transdermal delivery of sodium hyaluronate and other drugs. Safety was also confirmed through cytotoxicity tests and skin tissues analyses. Moreover, the augmentation of niacinamide delivery was verified through human experiments. The results demonstrate the tremendous potential of SEFM for skin electroporation in facial healthcare applications.

2. Results

2.1. Display and Mechanism of the SEFM

Figure 1a illustrates the method of using SEFM for skin electroporation. First, the medication mask with drugs is applied to the skin, which is made from wood pulp fibers with excellent water-absorbing properties. Then, the SEFM is worn through the ear hooks to ensure a secure attachment to the face. Finally, a controller composed of circuits and a battery is connected to the front of the SEFM, utilizing two connection points situated on the forehead. The silicone layer of the SEFM ensures excellent flexibility, stretchability, and conformity to complex curved surfaces, while the design of the ear hooks ensures strong fit between the SEFM and the face. From Figure 1b, it can be observed that the controller is magnetically adsorbed onto the outer side of the SEFM device and is connected to the inner electrodes of the SEFM. As shown in Figure 1c, these inner electrodes are a pair of serpentine network electrodes prepared from conductive ink, when the controller applies voltage to the skin through this electrode pair, drug delivery into the skin will be facilitated. The controller (Figure 1d) is composed of a printed circuit board (PCB) and a small-sized battery, and includes a control area and two connection points. The disassembly diagram, component display and circuit diagram of the controller can be found in Figures S2 and S3 (Supporting Information), with relevant explanations provided in Note S2. The functions of the control area are as follows: 1 (-) for reducing voltage amplitude, 2 (+) for increasing voltage amplitude, and 3 (M) for switching electrical pulse modulation, which can modify the voltage amplitude and frequency of the electrical pulse signal. The generated electrical pulse excitation waveform is shown in Figure 1e, in the form of square wave pulses with amplitude ranging from level 1 to level 6, increasing gradually. The voltage amplitude of level 6 is ≈50 V to 190 V (corresponding to the surface resistance of the skin, which varies from 2 to 500 kΩ due to different degrees of wetness), and the pulse width is 200 µs.

Y. Su
Beijing Key Laboratory of Engineered Construction and Mechanobiology
Institute of Mechanics
Chinese Academy of Sciences
Beijing 100190, China

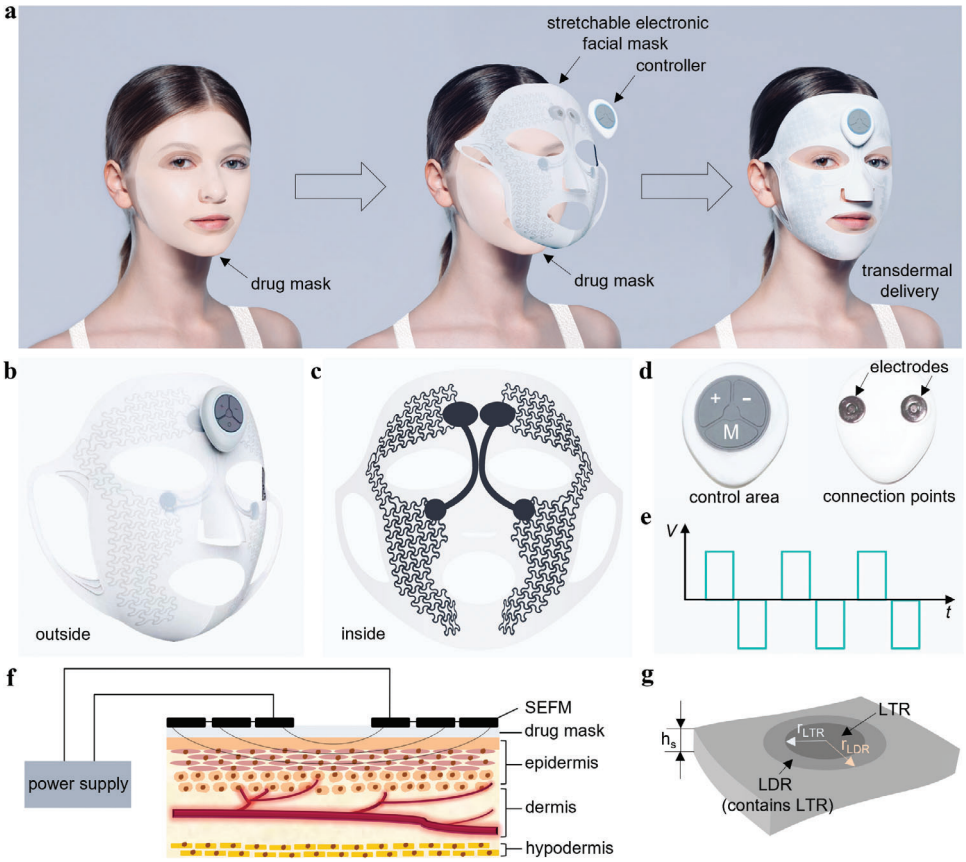

Figure 1. Display and mechanism of the SEFM. a) Schematic illustration of the use of the SEFM. b) Outside and c) Inside view of the SEFM. d) Controller, include control area and connect points (CPs). e) Impulse waveform, square wave pulse, ± 60 V, pulse width 200 µs. f) Schematic illustration of the underlying mechanism of skin electroporation by the SEFM. g) The LTR region and LDR region. $r_{LDR} = 30 - 500$ µm, $r_{LTR} = 10 - 300$ µm.

Figure 1f illustrates the basic mechanism of skin electroporation using the SEFM. The SEFM generates an electric field on both sides of the face, and if the skin is exposed to this electric field, the field is confined within the stratum corneum.[24–26] If the voltage on the stratum corneum reaches ≈60 V, it is highly likely that skin electroporation-related electrical breakdown occurs,[26] which exhibits a high degree of localizability. The local dissipation region (LDR) (Figure 1g) is the region where electrical breakdown typically occurs.[27] In this region, with a radius of r_{LDR} (≈30–500 µm), the electric field causes charge accumulation and separation, resulting in a significant decrease in the internal resistance of the medium by about four orders of magnitude.[27] The stratum corneum contains ≈100 series-connected bilayers, with a transmembrane potential of 0.3–1.0 V per layer, corresponding to a transdermal voltage range of 30–100 V, which is consistent with the range observed in cell electroporation experiments.[28] The local transmission region (LTR) (Figure 1g) is a smaller region located at the center of the LDR,[26–27,29,30] with a radius of r_{LTR} (≈10–300 µm). It is the core region of reduced resistance and typically exhibits higher conductivity, allowing for the transport of small ions (such as Na^+, Cl^-, Ca^{2+}) and large molecules within this region.[26,29] The current experimental evidence strongly supports a specific hypothesis that pulsed electric fields create "straight-through aqueous pathways" within the LTR,[28] enabling molecules to traverse the lipid bilayers of the skin's stratum corneum and pass through the hydrated corneocytes' interior. In summary, skin electroporation increases cell membrane permeability, thereby enhancing the quantity and depth of drug delivery via the transdermal route.

2.2. Design and Fabrication of the SEFM

In the design of SEFM, the controller needs to be connected to the printed electrodes made of conductive ink. Achieving a conductive connection and encapsulation between materials with a rigid-flexible interface of this kind, is a crucial technical challenge. This paper addresses this issue with two designs. 1) Using a magnet buckle to penetrate the silicone layer and conductive ink (**Figure 2a**), achieving a conductive connection between the controller and the conductive ink electrodes. The magnet buckle then passes through the stator (made of stainless steel) and the connector, and the two legs of the magnet buckle are bent outward until they are parallel to the stator's direction, securely fastening the penetrated components together and ensuring a reliable conductive connection. The stator serves to reduce stress concentration during the use of the magnet buckle. Without the stator, the stress will concentrate in the area corresponding to the two legs of the magnet buckle (Note S3 and Figure S4, Supporting Information). 2) The silicone cover is adhered to the assembled

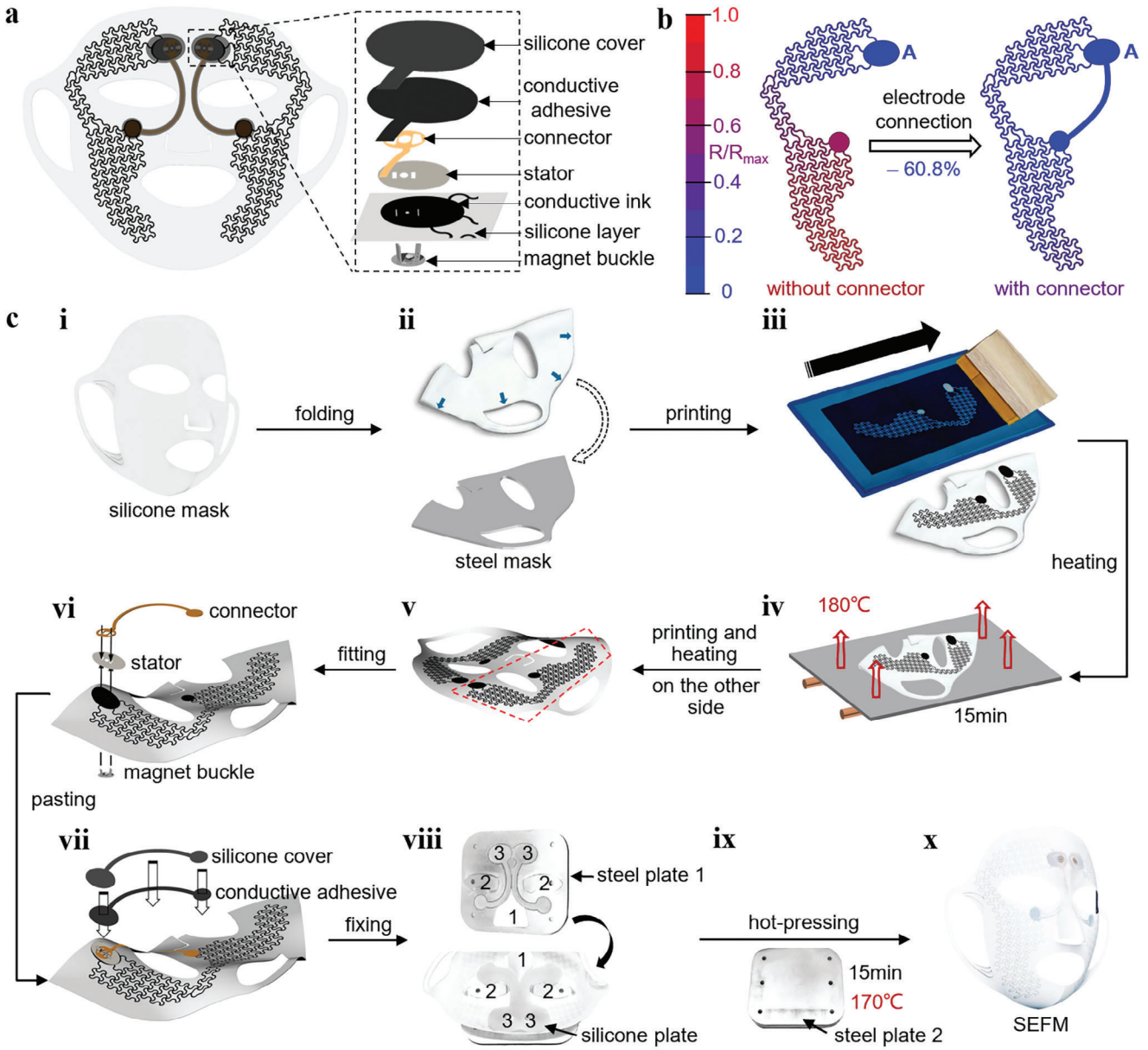

Figure 2. Design and fabrication of the SEFM. a) Disassembled illustration of the SEFM device structure. b) Normalized resistance distribution contour map of the printed circuit from various points to point A before and after the addition of electrode connections, obtained through finite element analyses. c–i–iii) print conductive pattern on one side of silicone mask by silk-screen printing, iv) place the silicone mask with printed pattern in the heating oven at 180 °C for 15 min, and repeat ii–iv) on the other side of the silicone mask, v–vi) passed the magnet buckle through the center of the conductive ink connection area connect with stator and connector above, and use the clamp fasten them together, vii) corresponding the position of the connector, add the silicone cover through conductive, viii) fix silicone on steel plate 1 with convex grooves 1–3, ix) place the steel plate 2 with six positioning cylinders align with the positioning holes on the steel plate 1, hot-press at 170 °C for 15 min, and x) the SEFM device.

components above using conductive adhesive, providing effective encapsulation.

On the other hand, in order to achieve a strong adhesion of the conductive ink to the silicone surface, a high-viscosity additive was introduced during the preparation of the conductive ink, resulting in higher resistance values of the printed electrodes. When using the controller to apply voltage to the face through the printed electrodes, an uneven distribution of electrical potential occurs, presenting another crucial technical challenge that needs to be addressed. To achieve a uniform potential distribution, this paper implements a conductive connection (Figure S5a, Supporting Information) between the upper and lower parts of the electrode area through a pair of connectors (made of copper). The design effectiveness was verified through simulation analysis using COMSOL software, as shown in Figure 2b. By calculating the resistance values from 112 points to point A, the resistive distribution color maps for electrode with and without connector were obtained. The maximum resistance value from the electrode with

connector to point A decreased by 60.8%, compared to the electrode without connector. At the same time, electrodes with connectors exhibit less variation in resistance values across the entire mask region (Figure S5b, Supporting Information), resulting in a more uniform potential distribution when the electrodes are energized.

The preparation process is illustrated in Figure 2c. i) The silicone raw materials and additives are mixed and poured into a mold, followed by hot-pressing and baking. Afterward, the silicone is taken out from the mold, and excess parts are removed to obtain the silicone mask. The silicone mask is symmetric at the center and can be unfolded into a plane after folding. ii) The silicone mask is wrapped around a steel mask and stretched to its outer edge, ensuring a flat surface. iii) Conductive ink is screen-printed on one side of the silicone mask. Ensuring strong bonding with the conductive ink to the silicone layer and maintaining good conductivity pose challenging issues, which will be further discussed in subsequent sections. iv) The silicone mask with printed conductive ink electrodes is removed from the steel mask and placed in a heating oven at 180 °C for 15 min until the conductive ink is completely cured. The steps (ii-iv) are repeated to process the other side of the silicone mask. v) The silicone mask with electrodes printed on both sides is unfolded. (vi) A magnet buckle is used to connect the silicone layer, conductive ink, stator, and connector by passing through them. vii) Conductive adhesive is applied to encapsulate this section of the components, bonding the silicone cover above the connector. This is another challenging issue, which will be detailed in subsequent sections. viii) The silicone mask, with conductive ink and other components added, is affixed to steel plate 1. Area 1 of the steel plate is hollow to accommodate the nose part of the silicone mask, area 2 contains two protrusions to secure the entire assembly through the eye part of the silicone mask, and area 3 has a pair of concave grooves that match the shape of the silicone cover for proper placement. ix) There are six positioning holes on steel plate 1, which are aligned and fixed with six positioning columns on steel plate 2. Then, they are hot-pressed at 170°C for 15 min to fully cure the conductive adhesive. x) The SEFM is prepared. The material cost for preparing a single SEFM is only 33 Chinese Yuan (CNY), and this low-cost component, coupled with high-yield manufacturing techniques, along with its inherent ease of use, is advantageous for individuals across various income levels.

2.3. Preparation and Electrical Performance of Conductive Ink

This study employs a highly stretchable and water-resistant silicone as the substrate for the SEFM. Silicone typically possesses low surface energy, making it challenging to adhere to other materials and form tight physical or chemical bonds. On the other hand, the silicone surface is enriched with silicone oil, rendering it smoother and less prone to adhesion with other materials.[31,32] Currently, widely studied water-based conductive inks[33–35] face challenges in adhering to the surface of silicone. Materials with higher viscosity, such as conductive silver paste[36–38] and conductive silver adhesives,[39,40] can accumulate on the surface of silicone to form electrodes. However, during the stretching of silicone, these materials tend to fracture, making it difficult to maintain their conductivity. Ensuring the adhesion of conductive ink to the surface of silicone and maintaining stable conductivity during silicone deformation is a challenge that needs to be overcome.

We propose a solution to modify conductive ink materials and design the mechanical structure of patterns after screen printing to overcome the aforementioned challenges. **Figure 3**a presents the raw materials of the conductive ink, including carbon black, graphene, silicone oil, kerosene, and platinum catalyst, with the proportions of each component are shown in Table S1 (Supporting Information), and the functions of each component and the silicone oil compositions are described in Note S4 (Supporting Information). The mixed conductive ink of these five materials is shown in Figure 3b, appearing as a black viscous liquid. Figure 3c demonstrates the apparent viscosity of the conductive ink as a function of shear rate, exhibiting shear thinning behavior characteristic of pseudoplastic fluids. As conductive ink passes through the mesh of the screen, external pressure and motion are applied to the ink, generating shear forces within it. As a result, the shear rate increases, causing the viscosity of the conductive ink to decrease. This allows it to flow more easily through the mesh of the screen during the printing process and ensures even distribution on the substrate when printed, leading to high-quality printing result.

In this proposed solution, we achieved excellent mechanical and electrical performance of silicone-based conductive ink electrodes through four design strategies: 1) Introduction of silicone oil material. The conductive ink adheres firmly to the silicone surface, necessitating good adhesion or crosslinking between the two. Silicone oil shares similar chemical properties with silicone and can cure and crosslink on the surface of silicone at high temperatures, resulting in strong adhesion. On the other hand, silicone oil maintains flexibility and elasticity after curing, ensuring that the conductive ink electrodes can deform with the silicone during stretching. SEM images displayed conductive carbon particles encapsulated by cured silicone oil, allowing these particles to deform alongside the silicone substrate without cracking (Note S5 and Figure S6, Supporting Information). Simultaneously, peel-off experiments validated the conducted adhesion strength, as the proportion of silicone oil in the conductive ink increased, the adhesion strength between the conductive ink and the silicone substrate significantly improved (Note S6 and Figure S7, Supporting Information). 2) Materials grinding. Directly mixing ink raw materials result in moderate conductivity in the cured ink because conductive particles struggle to form a dense conductive network post-curing. Grinding, however, promotes the formation of the conductive network. This can be represented by Figure 3d, which illustrates that the carbon black nanoparticles aggregate into larger clusters before grinding, resulting in a sparser conductive network after curing. Conversely, after grinding with a three-roll grinder, the carbon black particles transform from larger clusters into smaller ones, with an increased number of clusters. This leads to the formation of a denser conductive network after curing, thereby increasing the ink's conductivity. The scanning electron microscope images of cured ink before and after grinding are shown in Figure 3e, where the surface of the cured ink appears rough with larger particle diameters before grinding, while it becomes relatively smooth with smaller particle diameters after grinding.[41–43] The size of the clusters is reduced to below 5 µm, as measured by a scraping fineness meter (Figure 3f), and simultaneous SEM images indicate

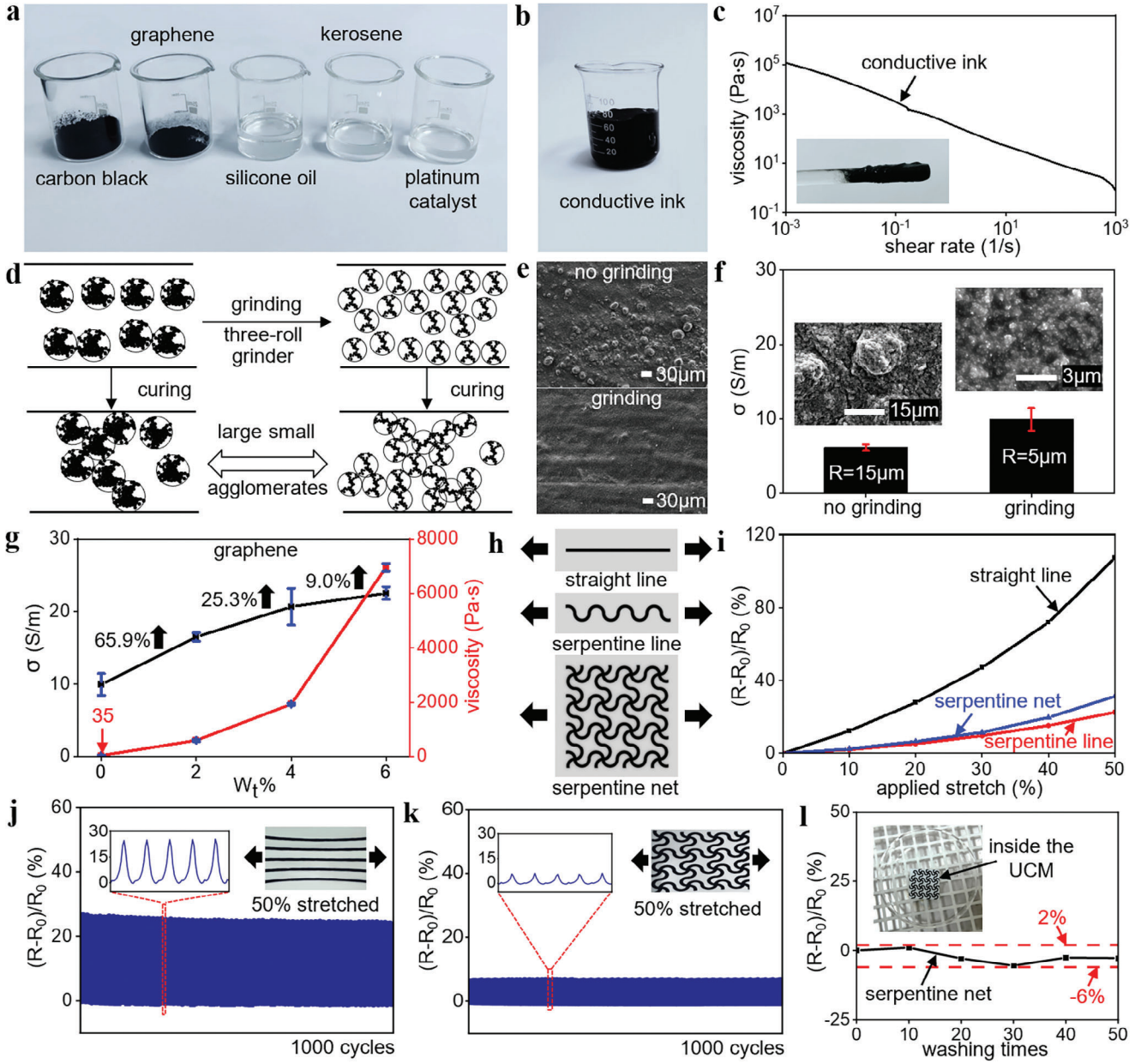

Figure 3. Preparation and electrical performance of conductive ink. a) Raw materials for conductive ink. b) Conductive ink. c) Experimental variation of apparent viscosity of conductive ink with shear rate. d) Illustration of the grinding process of conductive ink. e) Scanning electron microscope (SEM) images of conductive ink before and after grinding. f) Conductivity of conductive ink before and after grinding. g) Conductivity values and viscosity of conductive ink samples with varying graphene proportions. h) Demonstration of different printing patterns with applied displacement direction in finite element simulations. i) Finite element analyses of relative resistance changes for three patterns from 0% to 50% stretching. j) 50% tensile fatigue experiment of straight-line pattern sample, repeated 1000 times. k) 50% tensile fatigue experiment of serpentine net pattern sample, repeated 1000 times. l) 50 cycles of ultrasonic cleaning test in the Ultrasonic Cleaning Machine (UCM).

that the cluster size has reached below 3 μm. Correspondingly, the conductivity of the printed samples increased by 61.6%, with the dimension parameters of the test samples shown in Figure S8 (Supporting Information). 3) Introduction of graphene material. Graphene, as an exceptionally excellent conductive material, with its honeycomb-like arrangement in a 2D structure, allows electrons to move at high speeds. When combined with carbon black material, it can form composite materials with various conductive pathways. In the experiment, graphene is added in proportions ranging from 0% to 6%, with the other four components adjusted accordingly. The materials are then ground, screen printed, and thermally cured, as depicted in Figure 3g. When the graphene content increases from 0% to 2%, its conductivity increases by 65.9%. When it increases from 2% to 4%,

the conductivity increases by 25.3% compared to the conductivity at 2%. When it increases from 4% to 6%, the conductivity increases by 9.0% compared to the conductivity at 4%. Although increasing graphene content effectively enhances the conductivity of the conductive ink, adding an excessive amount of graphene will elevate the viscosity of the conductive ink (Figure 3g), leading to the issue of uneven distribution after printing, which affects the formation of patterns. Therefore, considering the acceptable balance between the viscosity of conductive ink and the magnitude of conductivity, 2% by weight of graphene was chosen as the preferred ratio for the conductive ink formulation. Viscosity experiments of the conductive ink and printed samples with different graphene proportions can be found in Figures S8 and S9 (Supporting Information), and the corresponding analyses is available in Notes S7 and S8 (Supporting Information). 4) Serpentine structure design. The conductive ink electrodes designed with a serpentine structure has curved portions that can disperse stretching strain, resulting in minimal overall resistance variation during stretching. As shown in Figure 3h, three patterned conductive ink electrodes were designed for finite element analyses (Note S9 and Figure S10, Supporting Information), and as depicted in Figure 3i, compared to the straight line, both the serpentine line and serpentine net exhibit significantly smaller relative resistance changes after stretching. The serpentine net shows a slightly larger change compared to the serpentine line. This is because during the stretching process, the vertically arranged lines in the serpentine net also undergo resistance changes. A comparative experiment was conducted using the serpentine net and straight-line patterns, as shown in Figure 3j,k. The conductive ink-silicone samples with linear patterns were subjected to 1000 cycles of 50% tensile fatigue testing using a tensile machine, and the resistance of the entire line was measured. When conductive ink-silicone samples were stretched from 0% to 50%, the resistance of the straight-line pattern increased by 25.1%, while the resistance of the serpentine net pattern increased by only 6.2%. After fifty cycles of ultrasonic cleaning, each lasting 3 min at 100% power and 40 kHz, it was observed that the electrical performance of the serpentine net electrode remained stable, with resistance variations not exceeding ±6% (Figure 3l). For detailed experimental procedures and sample parameter information refer to Figure S11 and Note S10 (Supporting Information). Meanwhile, during usage, the contact resistances between serpentine net electrodes and the skin are significantly lower than their respective self-resistances (Note S11 and Figure S12, Supporting Information). In summary, we have developed a water-resistant conductive ink electrode based on silicone substrate, which exhibits excellent mechanical properties and stable electrical performance.

2.4. Electrical and Mechanical of Performances of the Conductive Adhesive

During the preparation of SEFM, it is necessary to bond the conductive ink and copper connectors and encapsulate the connecting area. However, using adhesive containing alcohol components for encapsulation may lead to the swelling of conductive ink.[44,45] Specifically, during the encapsulation process, when alcohol substances from the adhesive penetrate into the conductive ink, the conductive ink absorbs them, resulting in swelling (Note S12 and Figure S13, Supporting Information). This swelling affects the conductive network already formed within the conductive ink. Since the size and quantity of conductive particles in the conductive network are fixed, the swelling disrupts the dense conductive network, leading to a decrease in the conductivity of the conductive ink, as shown in **Figure** 4a. This phenomenon was verified using a super-depth 3D surface profiler. The height distribution at positions y1 to y4 was obtained, as shown in Figure 4b. The left side of the ink surface was coated with adhesive, while the right side was not. The results, shown in Figure 4c,d, revealed a thickness difference of 42.59–41.27 µm on the left side and 27.19–34.72 µm on the right side. The significantly increased thickness on one side indicated swelling of the ink on that side. To address this issue, we devised a novel approach by incorporating conductive carbon black into high-temperature vulcanized silicone, which we refer to as conductive silicone. During the high-temperature curing process, the conductive silicone undergoes vulcanization, leading to a certain degree of volume expansion. Simultaneously, as the conductive ink swells, a conductive layer spontaneously forms on the surface by the conductive silicone. This conductive layer establishes a connection with the adjacent unbounded areas of conductive ink, and the connection ensures the continuous conductivity of the swollen region. The bonding process of the conductive adhesive is depicted in Figure 4e. After separating the conductive ink bonded with the conductive adhesive and measuring its resistance, it was found to be higher than that of the unbonded ink (Figure 4f). This confirms that the increased conductivity in the swollen region is due to the parallel effect of the newly formed conductive layer, rather than carbon black infiltration into the underlying conductive ink.

Subsequently, experimental verification was conducted. A rectangular area with four repeating units was cut from the SEFM, as shown in Figure 4g. A square silicone cover was then bonded to the rectangular area using conductive silicone, high temperature vulcanized (HTV) adhesive, and normal temperature vulcanized (NTV) adhesive. Among these three adhesives, both conductive silicone and high-temperature vulcanized (HTV) adhesive cure at 170°C for 15 min, while the curing condition for normal-temperature vulcanized (NTV) adhesive is at room temperature for 12 h. The resistance changes of the test points before and after bonding are depicted in Figure 4h. After HTV and NTV bonding, the resistance of the conductive ink increased by 40% and 31% respectively. However, the resistance decreased by 23% when bonded with conductive silicone. Mechanical properties of the conductive silicone were also tested, and the bonding strength of the three adhesives under T-type stretching was analyzed, as shown in Figure 4i. The test samples were rectangular silicone pieces measuring 150 mm in length, 20 mm in width, and 0.3 mm in thickness. The results, presented in Figure 4j, demonstrated that conductive silicone exhibited the highest bonding strength, followed by HTV. The silicone attached with NTV adhesive experienced debonding during the stretching process, indicating the lowest bonding strength. Furthermore, an ultrasonic cleaning test was conducted on the sample shown in Figure 4k to confirm its wash resistance, the resistance change during 50 cycles of ultrasonic cleaning remained within 3%. The use of conductive silicone for connecting the printed circuit and

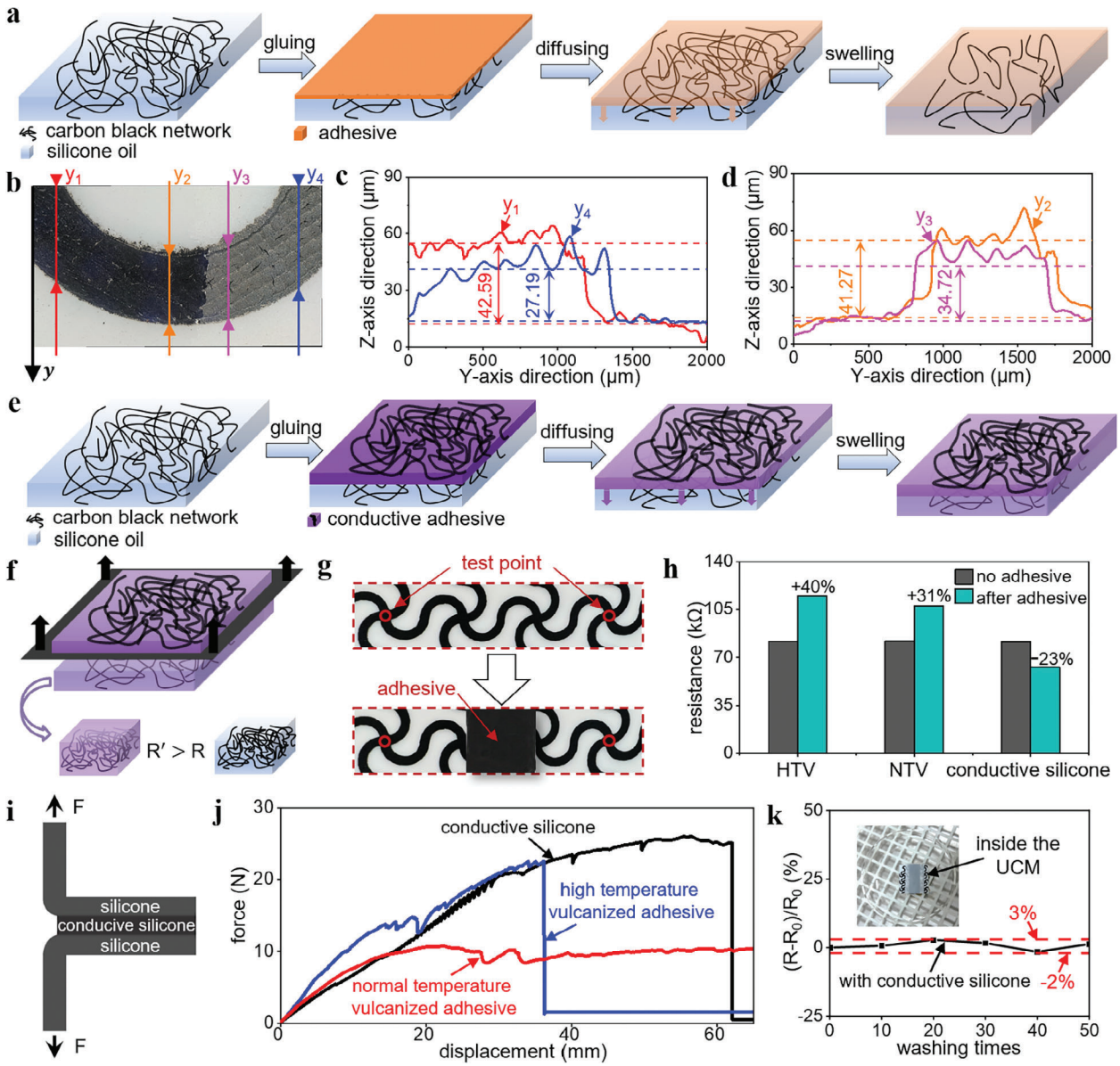

Figure 4. Electrical and mechanical performances of conductive adhesive. a) Printed circuit of carbon black conductive ink bonded with nonconductive adhesive, leading to ink swelling and damage to the formed carbon black conductive network. b) Carbon black conductive ink sample coated with nonconductive adhesive on the left side, with height distribution obtained for positions y1 to y4 using a super depth-of-field 3D surface profiler. c) Height distribution of y1 and y4. d) Height distribution of y2 and y3. e) Printed circuit of carbon black conductive ink bonded with conductive adhesive, where ink swelling occurs simultaneously with the formation of a conductive layer on the surface of the conductive ink. f) Peeling of the bonded conductive layer in (e), showing higher resistance of the underlying swollen conductive ink compared to the unswollen conductive ink. g) Samples for bonding tests. h) Resistance changes of the test points before and after the bonding tests. i) T-type peeling experiment of the conductive adhesive. j) Tensile strength comparison of the three adhesives. k) 50 cycles of ultrasonic cleaning test in the UCM.

the metal circuit ensured stable electrical and mechanical connections under deformation, unaffected by washing. Another ultrasonic cleaning test was also conducted on the entire SEFM device (Figure S11 and Note S10, Supporting Information), the results showed that during 50 cycles of ultrasonic cleaning, the resistance changes for multiple test points remained within ±8%. As a drug delivery device, its most common usage involves repeated washing before and after use. From this perspective, the SEFM device demonstrates good reusability.

2.5. Animal Experiment on Transdermal Drug Delivery Using SEFM

Sodium hyaluronate (SH), aloe powder, β-glucose, and D-panthenol are widely used for improving facial skin health, and can also be applied in the treatment of skin diseases. They possess moisturizing, anti-inflammatory, antibody production promotion, and metabolic enhancement properties, respectively. Among these substances, β-glucose has a molecular weight of

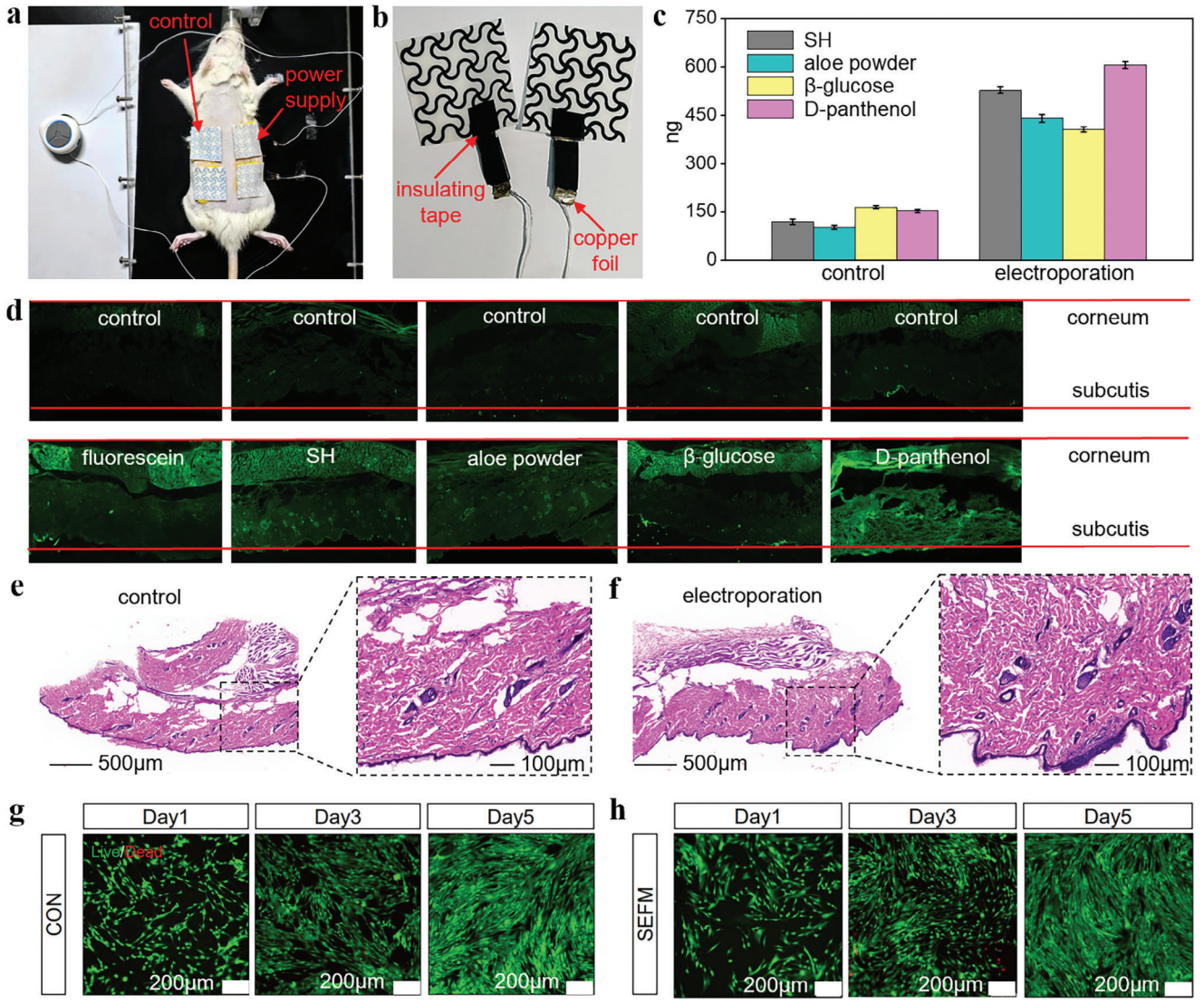

Figure 5. Animal experiment on transdermal drug delivery using SEFM. a) Schematic diagram illustrating the positioning of the device during the SEFM transdermal drug delivery experiment conducted on rats. b) Electrode samples used in the experimental group. c) Comparison of the total amount of drug delivered under skin electroporation for different drugs. d) Comparison of the penetration depth of different drugs. e) Histological sections of the control group's animal tissues. f) Histological sections of animal tissues in the skin electroporation experimental group, demonstrating the integrity of the epidermis and dermis. g) Live/dead staining results of human dermal fibroblasts in the control group ($n = 3$). h) Live/dead staining results of human fibroblasts cocultured with SEFM, indicating the noncytotoxicity of SEFM ($n = 3$).

≈200 Da, while hyaluronic acid has a molecular weight of about 5 million Daltons, and all four of these substances are highly hydrophilic. Researching the transdermal delivery effects of these four substances through skin electroporation holds a certain degree of representativeness, as it can provide insights into the effects on both small-molecule and large-molecule hydrophilic substances. To validate the enhancing effect of skin electroporation SEFM on the transdermal delivery of these four substances, a controlled experiment was conducted on an animal model of 5 SPF-grade Sprague–Dawley rats (6–8 weeks old). First, the four drugs were labeled with 0.1% fluorescein, impregnated onto fabric, and placed on the dorsal skin of the rats, covered with SEFM for conformal fit, as shown in **Figure** 5a. The left pair of electrodes served as the control group, while the right pair of electrodes represented the experimental group. The electrodes in the experimental group, as depicted in Figure 5b, featured a 3 × 3 serpentine electrode array pattern connected to copper plates using conductive gel and insulated with insulating tape. In Figure 5a, within the experimental group on the right side of the rat's back, a pulse stimulation voltage with an amplitude of 100 V was applied. Each individual pulse had a pulse width of 200μs, with an interval of 60 ms between each set of pulses. Additionally, there was a pause of 0.7s after every 8s of continuous operation in this pattern, which lasted for 15 min. The waveform and parameters of the pulse voltage can be found in Figure S14 (Supporting Information), and further detailed explanations are provided in Note S13 (Supporting Information). The control group electrodes were not subjected to any stimulation voltage. After the

experiment, the rats were euthanized, and the skin at the application site was excised with sterile surgical scissors to prepare skin tissue samples. Initially, the quantitative analysis of drug components in the skin was conducted using high-performance liquid chromatography (HPLC). Figure 5c demonstrates that in the absence of skin electroporation, the amount of drug entering the skin was minimal, not exceeding 200 ng. In contrast, the experimental group that received electrical stimulation exhibited a three to four-fold augmentation in drug penetration into the skin. Additionally, to provide a more visual representation, skin slices were observed and photographed under a fluorescence microscope to compare the depth of drug penetration, as shown in Figure 5d. The experimental groups for all four drugs exhibited increased penetration depth and brighter fluorescence compared to their respective control groups, indicating that electrical stimulation facilitated fluorescein penetration. Among the four drugs, D-panthenol exhibited the highest penetration depth, reaching the dermis, confirming the effectiveness of skin electroporation drug delivery. The experiments mentioned above have confirmed that skin electroporation can increase the amount of drug delivered to the skin by 3–4 times and significantly enhance the depth of drug penetration.

On the other hand, hematoxylin-eosin staining was performed to assess whether the skin electroporation device caused any damage to the skin tissue. As depicted in Figure 5e,f, the skin tissue of the group with skin electroporation (experimental group) showed no difference compared to the control group (no skin electroporation group), suggesting that skin electroporation does not harm the skin. Furthermore, the biocompatibility of SEFM with fibroblasts was investigated, as shown in Figure 5g,h. The cellular cytotoxicity was performed by live/dead assay and cck8 test after 1, 3, and 5 days of co-cultivation with SEFM. The results indicate that the survival rate of fibroblasts cultivated on SEFM materials during the 1–5 day was as high as 95–97%, which is very close to the 97–98% of the control group (Figure S15a, Supporting Information). This suggests that fibroblasts can survive well on SEFM materials. The specific calculation process and figures can be found in Note S14 and Figure S16 (Supporting Information). In addition to comparing the survival rates of the cells, we also compared the cell proliferation numbers. Over the course of 1, 3, and 5 days, the fibroblasts cultivated on SEFM continued to proliferate, with an increase from 100% on the first day to 200% on the third day and 400% on the fifth day (Figure S15b, Supporting Information). While the growth rate was not as high as that of the control group (no SEFM materials) which increased from 100% to 240% to 480%, it still indicates that SEFM materials are friendly to cell proliferation. Overall, these results demonstrate the outstanding biocompatibility of SEFM, and the 15-min electroporation did not cause tissue damage. These experiments validate the biocompatibility of SEFM materials and the safety of skin electroporation on skin tissues.

2.6. Human Experiment of Nicotinamide Transdermal Delivery by the SEFM

After animal experiments, we recruited 2 volunteers for our study. Due to variations in facial shapes and sizes, it was impractical to conduct a control experiment on the entire face. Therefore, we selected the inner forearms as the site for drug delivery. Nicotinamide, also known as vitamin B3, is a vitamin that is particularly effective when applied topically to treat or improve localized skin conditions such as acne, eczema, and inflammation, compared to oral or injectable methods. As shown in **Figure 6**a, a 40 mm × 40 mm area on the left forearm of each volunteer was applied with a nicotinamide water aqua mask as the control group, while a similarly sized area on the right forearm was applied with a nicotinamide water aqua mask or oil-in-water mask and subjected to 15 min of skin electroporation as the experimental group. The difference between the water aqua mask and the oil-in-water mask lies in the solvent used in the latter.

In this section, it is necessary to investigate the delivery of nicotinamide into the volunteers' forearm skin. Confocal Raman spectroscopy is a nondestructive technique that does not require skin puncture or tissue sample collection. This allows the research in this section to be conducted without compromising the integrity of the skin, thereby reducing discomfort and risk to the volunteers. To validate the effectiveness of confocal Raman spectroscopy in detecting the presence of nicotinamide, we conducted Raman spectroscopy measurements and comparisons of various substances in advance, and the spectra can be found in Figure S17 (Supporting Information). The results of the measurements demonstrated distinct differences in the Raman spectra of the 5% nicotinamide water aqua mask solution and water aqua solution, as well as between the 5% nicotinamide oil-in-water mask solution and oil-in-water solution. Furthermore, there were significant differences in the Raman spectra characteristic peaks between these four substances and the skin. This indicates that substances can be distinguished based on the positions of characteristic peaks in the Raman spectra, and their content can be estimated based on the height of the corresponding characteristic peaks. The 2 volunteers were assigned to two separate groups. Volunteer A used the 5% nicotinamide water aqua mask, while volunteer B used the 5% nicotinamide oil-in-water mask. Prior to the experiment, the volunteers cleaned their inner forearms with water and waited for 30 min in a controlled temperature and humidity environment. During the experiment, skin electroporation with a voltage amplitude at level 6 was applied to the right forearm, while the left forearm received no electrical stimulation. Measurements of skin barrier thickness, nicotinamide permeability, and skin hydration were conducted before and after the electrical stimulation. The analysis of skin barrier thickness was based on the distribution of thickness and hydration in the stratum corneum. As shown in Figure 6b, compared to the nonstimulated control group, both the 5% nicotinamide water aqua solution and the 5% nicotinamide oil-in-water solution resulted in an increase in skin barrier thickness following skin electroporation. The permeability curve of the 5% nicotinamide water aqua solution after skin electroporation is shown in Figure 6c, indicating a significant increase in the depth of penetration of the solution within the skin, up to 10 μm, with an increase of 34.2%. The total permeability of the 5% nicotinamide water aqua solution increased by 39.8%, as shown in Figure 6d. The water content increment at 8 μm below the skin surface rose by 67.8% following skin electroporation, as depicted in Figure 6e. Similarly, the permeability curve of the 5% nicotinamide oil-in-water solution after skin electroporation is illustrated in Figure 6f, showing a significant increase in the depth of

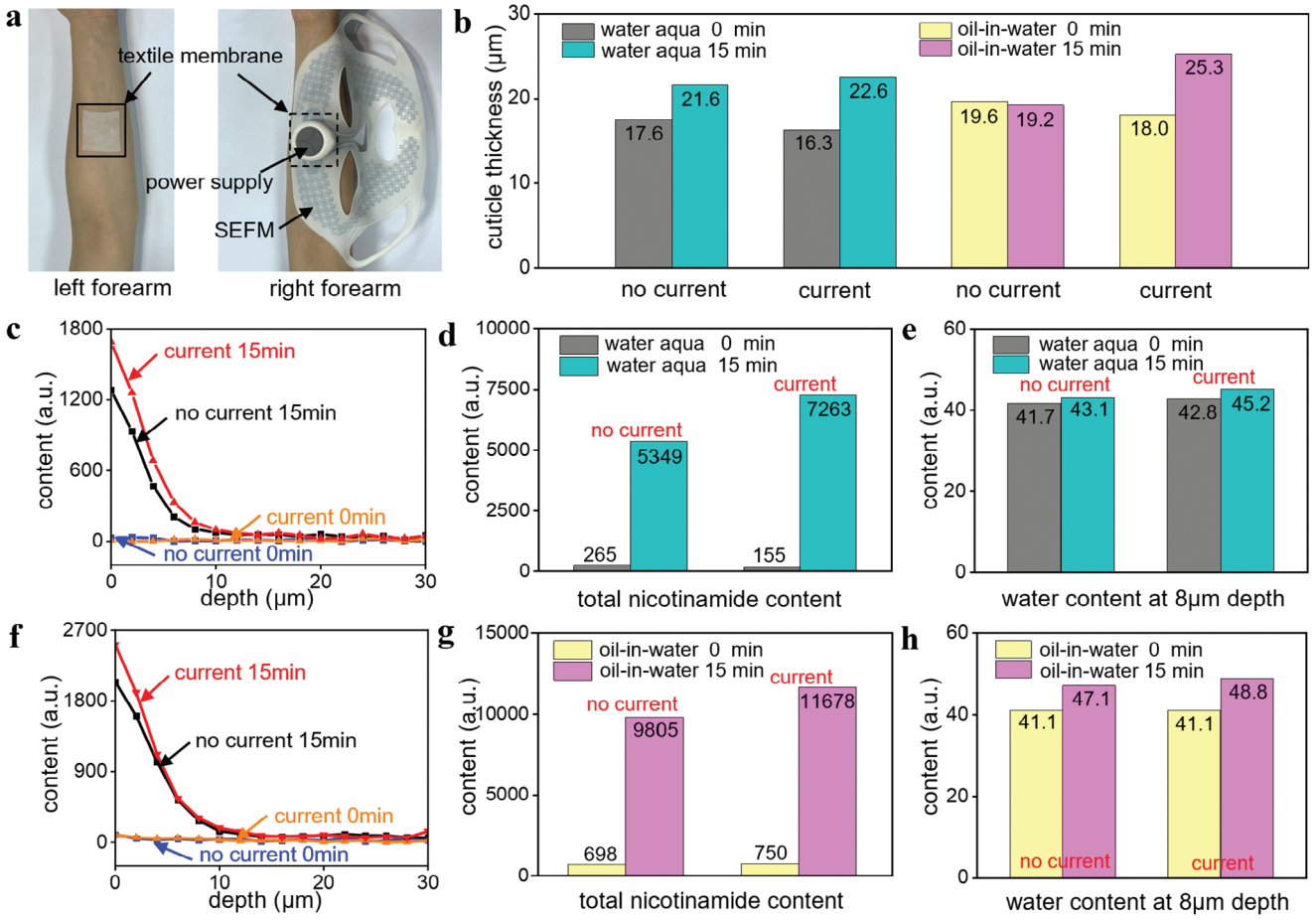

Figure 6. Human experiment of transdermal delivery of nicotinamide by SEFM. a) SEFM transdermal delivery of nicotinamide conducted on the inner forearms of the subjects. b) Thickness of the stratum corneum in the experimental and control groups after 15 min of application with 5% nicotinamide water aqua solution and 5% nicotinamide oil-in-water solution with skin electroporation. c) Nicotinamide permeability curves on the skin for 5% nicotinamide water aqua mask and 5% nicotinamide water aqua mask + skin electroporation. d) Nicotinamide content in the stratum corneum for the 5% nicotinamide water aqua mask experiment. e) Water content at 8 μm depth after the 5% nicotinamide water aqua mask experiment. f) Nicotinamide permeability curves on the skin for 5% nicotinamide oil-in-water mask and 5% nicotinamide oil-in-water mask + skin electroporation. g) Nicotinamide content in the stratum corneum for the 5% nicotinamide oil-in-water mask experiment. h) Water content at 8 μm depth after the 5% nicotinamide oil-in-water mask experiment.

penetration of the solution within the skin, up to 10 μm, with an increase of 24.4%. The total permeability of the 5% nicotinamide oil-in-water solution increased by 20.0%, as shown in Figure 6g. The water content increment at 8 μm below the skin surface rose by 27.9% following skin electroporation, as shown in Figure 6h.

These results demonstrate that skin electroporation promotes the penetration of nicotinamide into the skin, with both water aqua and oil-in-water solutions exhibiting increased permeability ranging from 20.0% to 39.8%. Furthermore, an increase in water content and an increase in stratum corneum thickness were observed in the superficial layer (8 μm) of the skin following skin electroporation. This once again emphasizes the efficacy of skin electroporation SEFM in enhancing transdermal drug delivery.

3. Conclusion

In summary, we introduce a stretchable electronic facial mask for skin electroporation by transdermal drug delivery, and SEFM offers features of reusability, water-resistant, low cost, and portability. To achieve these objectives while maintaining satisfactory mechanical and electrical performance of the device, we innovated in two main areas. 1) Mechanical design and modification of conductive ink. We initiated improvements in conductive ink by introducing silicone oil to enhance its adhesion to silicone, followed by material grinding and graphene doping to increase ink conductivity by 61.6% and 65.9%, respectively. Finally, we incorporated a serpentine net structure into the ink electrode design, which reduced the relative resistance change by more than 50% compared to the straight line structure after stretching, ensuring its stretch stability. In a fatigue test involving 1000 cycles of 50% stretching, the serpentine net ink electrode exhibited only a 6.2% change in resistance. Furthermore, after 50 cycles of ultrasonic cleaning, the resistance remained stable, demonstrating excellent mechanical performance and stable electrical properties. 2) Modification of conductive adhesive through high-temperature vulcanized silicone. To address the issue of ink swell during

encapsulation, we introduced carbon black into high-temperature vulcanized silicone. During the curing process, as the conductive ink expanded, the carbon black-doped conductive silicone spontaneously formed a conductive layer on its surface. This conductive layer established an electrical connection with adjacent unbounded areas of conductive ink, ensuring good conductivity within the expanded region. Experimental results indicated that after encapsulation with high-temperature vulcanized and normal temperature vulcanized adhesives, the resistance of the conductive ink increased by 40% and 31%, respectively. In contrast, encapsulation with conductive silicone reduced the ink resistance by 23%. Moreover, this encapsulation maintained stable resistance even after 50 cycles of ultrasonic cleaning.

Under these design and modification approaches, the SEFM achieved outstanding drug delivery performance. Through experiments with rats, we validated a 3–4 times increase in drug delivery amounts compared to the control group, along with significantly enhanced drug penetration depths for various substances. Biocompatibility tests confirmed the safety of SEFM materials, while tissue section analysis verified the safety of SEFM's skin electroporation. Additionally, in human volunteer experiments, SEFM demonstrated the ability to increase the introduction of 5% nicotinamide solution by over 20%, further affirming its efficacy in transdermal electrically stimulated drug delivery. These research findings underscore the significant potential of the developed SEFM for facial healthcare applications. Furthermore, the SEFM, based on silicone substrate and utilizing silk-screen printing and encapsulation processes, can be applied to other drug delivery devices or in the fabrication of flexible sensors. This SEFM platform holds promise for future integration of temperature and pressure sensing capabilities, in combination with techniques such as microneedle and ultrasound-assisted drug delivery, to enable multifunctionality. The SEFM platform is poised for further development toward commercialization, following a similar strategy.

4. Experimental Section

Finite Element Analysis of Resistance Distribution: In order to verify the effectiveness of incorporating copper connectors in addressing the issue of uneven potential distribution caused by large electrode area, finite element analysis was performed using the commercial software COMSOL (Figure 2b). The steady-state modeling was carried out by selecting the physics field "Current" in the "AC/DC" module. The CAD drawing of the serpentine printed circuit was imported into the COMSOL software, and a solid with a thickness of 0.02 mm, representing the conductive ink electrode, was created for the purpose of simulating its electrical properties (Figure S5c, Supporting Information). The material parameters are listed in Table S2 (Supporting Information) (some parameters were simplified for calculation purposes due to subsequent normalization). Subsequently, the electrostatic boundary conditions were defined, with side A grounded (Figure S5d, Supporting Information), and side N (Figure S5e, Supporting Information) set to have a terminal current of 1 A (in practice, 112 sides were uniformly selected and their terminal currents were set to 1 A for calculation. Here, side N is used as an example to show the results of a single calculation). The steady-state calculation was performed to obtain the potential distribution from side N to side A (Figure S5f, Supporting Information), and the resistance value from side N to side A was derived through global calculations of derived values. Then, the resistance values of all 112 sides to side A were calculated, followed by normalization, converting all obtained resistance values to a range of 0–1. The range of 0–1 was divided into 10 regions, and the colors of the color blocks in the red-blue gradient bar corresponding to each region were determined (Figure S5g, Supporting Information). The colors corresponding to the numbers were filled in the printed circuit diagram using CAD (Figure S5h, Supporting Information), resulting in a resistance distribution map from various points to side A before connection (Figure S5i, Supporting Information). Subsequently, the two connection points in the circuit were shorted (right side of Figure 2b), and the resistance values from 112 sides to side A were recalculated, repeating the aforementioned procedures. This yielded the changes in resistance distribution of the entire circuit before and after connection (Figure 2b).

Printing and Measuring the Resistance of Conductive Ink: A 200-mesh screen was prepared to compare the conductivity of the ink under different conditions. A fine line measuring 30 mm in length and 0.9 mm in width was printed on a silicone sheet (Figure S18a, Supporting Information). The sheet was then placed in a heating oven and heated at 180 °C for 15 min. The resistance value measured at the ends of the line segment using a multimeter is depicted in Figure S18b (Supporting Information) (detailed parameters refer to Note S8 and Figure S8, Supporting Information).

Fatigue Experiments of Printed Circuits: For the straight line printed circuit and serpentine net printed circuit, elongated samples were printed (Figure S18d,e, Supporting Information). The ends of the printed circuits were fixed using conductive silver adhesive (which required curing at 130 °C for 10 min). The printed samples were then folded at the ends (Figure S18c, Supporting Information), leaving a deformation area of 30 mm × 30 mm within the silicone. The portion held by the clamp was wrapped with silicone for insulation. At the same time, added double-sided PI tape inside the clamp to enhance the holding force. Subsequently, a fatigue experiment was conducted with 1000 cycles of 50% deformation.

Silk Screen Printing Process for the Circuit on the Mask: Using CAD, the serpentine interconnect structure was designed with the following basic parameters (Figure S19, Supporting Information): line width of 0.9 mm, outer arc radius of 2.45 mm, inner arc radius of 1.55 mm, length of three basic units in a single cycle of 28 mm, and width of 13.5 mm. The folded pattern of the silicone mask on one side was used as a reference for drawing the entire conductive network (Figure S20a, Supporting Information). A customized silk screen printing mesh was prepared, and the folded silicone mask was placed underneath the mesh and aligned properly (Figure S20b, Supporting Information). The ink was applied and printed, resulting in a grid-like pattern of ink after curing, as observed in the microscopic photographs (Figure S20c, Supporting Information).

Rheological Performance Testing of the Ink: The viscoelastic characteristics and other rheological behaviors of ink were measured by a HAAKE RS6000 rotational rheometer. A plate rotor sensor system P35 was chosen in this work. The diameter of rotor P35 is 35 mm, and the gap between the rotor and stage is 1 mm. The shear rate range of this rheometer is 0.001–1500 s^{-1}, and the viscosity range is 0.5–10^6 mPa s. A variety of temperature control units are available to handle experimental temperatures from 0 to 100 °C with an accuracy of 0.1°C. In this work, the experimental temperature is controlled in the range from 20 to 70 °C. The viscoelastic behaviors of ink were measured on the small amplitude oscillatory shear measurement method. The shear stress control test model (CS) was used in this study. In the CS model, the shear stress is assigned an amplitude and an angular frequency periodicity, and the corresponding strain is measured. A shear stress sweep with a constant frequency was first performed to obtain the linear viscoelastic region of ink. Then, a frequency sweep was performed to systematically measure the viscoelastic characteristics of a series of ink.

The Experiment on the Variation of Ink Swelling Thickness: The experiment was conducted at the Special Lubricants and Sealing Materials Group, Lanzhou Institute of Chemical Physics, with the participation of Wanxin Wei. A high-resolution confocal microscope (VHX-6000, Keyence) was employed for 3D surface profiling.

Rat Drug Delivery Experiment and Tissue Integrity Assessment: The experiment was conducted by Shanghai Qiansu Biotechnology Co., Ltd., and the detailed procedure can be found in Note S15 of the Supporting Information. The animal experiment was approved by the Institutional Review

Board at Institute of Mechanics, Chinese Academy of Sciences (Approval No. 202310).

Human Fibroblast Culture: The fibroblasts were cultured in Dulbecco's Modified Eagle Medium (DMEM) supplemented with 10% fetal bovine serum (FBS), 1% antibiotic-antimycotic, and 1% L-glutamine at 37 °C in a humidified atmosphere of 5% CO_2. When the cells reached ≈80% confluence, adherent fibroblasts were detached using 0.25% trypsin-EDTA (GIBCO) and passaged.

Cytotoxicity: *(1). Live/Dead Assay*: Cell viability survival rate was assessed using the Live/Dead kit (Yeasen, China). Briefly, cells were seeded in 48-well plates at a density of 6×10^4 cells mL^{-1}. The SEFM were added, and the cells were co-cultured under standard conditions at 37 °C with 5% CO_2. After incubation for 60 min at 37 °C, fibroblasts were stained using the Live/Dead kit according to the manufacturer's instructions on days 1, 3, and 5, respectively. The stained fibroblasts were examined using a fluorescence microscope (Nikon, Japan), with living cells appearing as emerald green and dead cells appearing as emerald red. *(2). CCK-8 Assay*: The cytotoxicity of on fibroblasts was evaluated using the CCK-8 assay (Beyotime, China) following the manufacturer's instructions. Cells were seeded in 48-well plates at a density of 6×10^4 cells mL^{-1}. The cells were cocultured as described above. On days 1, 3, and 5 of the experiment, CCK-8 solution (60 µL) was added to each well according to the instructions. The plate was then incubated in the dark at 37 °C for 1 h, and the optical density (OD) of the solution was measured at 450 nm using a microplate reader.

Niacinamide Transdermal Delivery Experiment on Volunteer's Arm: The experiment evaluated the enhancing effect of skin electroporation stimulation on niacinamide permeation in the skin using confocal Raman spectroscopy. Based on Figure S17 (Supporting Information), it can be concluded that there are significant differences between the test samples and skin spectra, indicating the potential for studying the permeability of target components. The experiment involving human volunteers was approved by the Institutional Review Board at the Institute of Mechanics, Chinese Academy of Sciences (Approval No. 202309), wherein the volunteers took part following informed consent.

Supporting Information

Supporting Information is available from the Wiley Online Library or from the author.

Acknowledgements

Y.S. gratefully acknowledges support from the National Natural Science Foundation of China (grant 12172359), Key Research Program of Frontier Sciences of the Chinese Academy of Sciences (ZDBS-LY-JSC014), and CAS Interdisciplinary Innovation Team (JCTD-2020-03).

Conflict of Interest

The authors declare no conflict of interest.

Author Contributions

Y.S. and X.X. conceived the concept. X.X., L.G., Z.Z., H.L., W.W., and J.Z. conducted the experimental fabrication, finite element analyses and performance tests. H.G., S.D. and Q.G. conducted the cellular cytotoxicity experiment. Y.L., L.G., Q.L., and C.L. participated in the figure preparation. Y.Y. conducted the human experiment. X.X., S.L., and Y.S. discussed all the data. X.X., Y.S., and S.L. prepared the manuscript. Y.S. supervised the project.

Data Availability Statement

The data that support the findings of this study are available from the corresponding author upon reasonable request.

Keywords

conductive ink, conductive silicone, skin electroporation, stretchable electronics

Received: September 14, 2023
Revised: October 29, 2023
Published online: November 21, 2023

[1] J. K. L. Tan, K. Bhate, *Br. J. Dermatol.* **2015**, *172*, 3.
[2] E. Orion, R. Wolf, *Clin. Dermatol.* **2014**, *32*, 767.
[3] R. H. Guy, *Handb. Exp. Pharmacol.* **2010**, *197*, 399.
[4] M. R. Prausnitz, R. Langer, *Nat. Biotechnol.* **2008**, *26*, 1261.
[5] A. Azagury, L. Khoury, G. Enden, J. Kost, *Adv. Drug Delivery Rev.* **2014**, *72*, 127.
[6] N. A. Charoo, Z. Rahman, M. A. Repka, S. N. Murthy, *Curr. Drug Delivery* **2010**, *7*, 125.
[7] A. Kovacik, M. Kopecná, K. Vávrová, *Expert Opin. Drug Delivery* **2020**, *17*, 145.
[8] R. Pereira, S. G. Silva, M. Pinheiro, S. Reis, M. L. d. Vale, *Membranes* **2021**, *11*, 343.
[9] P. Karande, S. Mitragotri, *Biochim. Biophys. Acta Biomembr.* **2009**, *1788*, 2362.
[10] P. Arpaia, U. Cesaro, N. Moccaldi, *Sci. Rep.* **2017**, *7*, 44647.
[11] V. Dhote, *Sci. Pharm.* **2012**, *80*, 1.
[12] G. Pontrelli, M. Lauricella, J. A. Ferreira, G. Pena, *Math. Med. Biol.* **2017**, *34*, 559.
[13] Y. Talbi, E. Campo, D. Brulin, J. Y. Fourniols, *Electron. Lett.* **2018**, *54*, 739.
[14] I. Lavon, J. Kost, *Drug Discovery Today* **2004**, *9*, 670.
[15] D. Park, J. Won, G. Lee, Y. Lee, C.-W. Kim, J. Seo, *Skin Res. Technol.* **2022**, *28*, 291.
[16] B. C.-Q. Seah, B. M. Teo, *Int. J. Nanomed.* **2018**, *13*, 7749.
[17] X. Hong, Z. Wu, L. Chen, F. Wu, L. Wei, W. Yuan, *Nano-Micro Lett.* **2014**, *6*, 191.
[18] S. D. Gittard, A. Ovsianikov, B. N. Chichkov, A. Doraiswamy, R. J. Narayan, *Expert Opin. Drug Delivery* **2010**, *7*, 513.
[19] J. W. Lee, J.-H. Park, M. R. Prausnitz, *Biomaterials* **2008**, *29*, 2113.
[20] A.-R. Denet, R. Vanbever, V. Préat, *Adv. Drug Delivery Rev.* **2004**, *56*, 659.
[21] S. Berko, K. F. Szucs, B. Balazs, E. Csanyi, G. Varju, A. Sztojkov-Ivanov, M. Budai-Szucs, J. Bota, R. Gaspar, *Drug Des. Devel. Ther.* **2016**, *10*, 1695.
[22] B. Zorec, J. Jelenc, D. Miklavcic, N. Pavselj, *Int. J. Pharm.* **2015**, *490*, 65.
[23] S. Li, J. Xu, R. Li, Y. Wang, M. Zhang, J. Li, S. Yin, G. Liu, L. Zhang, B. Li, Q. Gu, Y. Su, *ACS Nano* **2022**, *16*, 5961.
[24] P. M. Elias, *J. Controlled Release* **1991**, *15*, 199.
[25] P. M. Elias, *Drug Dev. Res.* **1988**, *13*, 97.
[26] U. F. Pliquett, G. T. Martin, J. C. Weaver, *Bioelectrochemistry* **2002**, *57*, 65.
[27] U. F. Pliquett, T. E. Zewert, T. Chen, R. Langer, J. C. Weaver, *Biophys. Chem.* **1996**, *58*, 185.
[28] J. C. Weaver, T. E. Vaughan, Y. Chizmadzhev, *Adv. Drug Delivery Rev.* **1999**, *35*, 21.
[29] M. R. Prausnitz, J. A. Gimm, R. H. Guy, R. Langer, J. C. Weaver, C. Cullander, *J. Pharm. Sci.* **1996**, *85*, 1363.
[30] U. F. Pliquett, R. Vanbever, V. Preat, J. C. Weaver, *Bioelectrochem. Bioenerg.* **1998**, *47*, 151.
[31] Z. H. Hu, M. L. Liao, Y. H. Chen, Y. P. Cai, L. L. Meng, Y. J. Liu, N. Lv, Z. G. Liu, W. E. Yuan, *Int. J. Nanomed.* **2012**, *7*, 5719.

[32] Y. Liang, N. Kociok, M. Leszczuk, W. Hiebl, B. Theisinger, A. Lux, A. M. Joussen, *Brit. J. Ophthalmol.* **2008**, *92*, 1522.
[33] Y. Z. N. Htwe, M. K. Abdullah, M. Mariatti, *J. Mater. Res. Technol.* **2022**, *16*, 59.
[34] S. Martinez-Crespiera, B. Pepio-Tarrega, R. M. Gonzalez-Gil, F. Cecilia-Morillo, J. Palmer, A. M. Escobar, S. Beneitez-Alvarez, T. Abitbol, A. Fall, C. Aulin, Y. Nevo, V. Beni, E. Tolin, A. Bahr, *Int. J. Mol. Sci.* **2022**, *23*, 2946.
[35] L. Sanchez-Duenas, E. Gomez, M. Larranaga, M. Blanco, A. M. Goitandia, E. Aranzabe, J. L. Vilas-Vilela, *Materials* **2023**, *16*, 3940.
[36] X. Liu, S. Wu, B. Chen, Y. Ma, Y. Huang, S. Tang, W. Liu, *J. Mater. Sci.: Mater. Electron.* **2021**, *32*, 13777.
[37] A. A. Wereszczak, M. C. Modugno, B. R. Chen, W. M. Carty, *IEEE Trans. Compon. Packaging Manuf. Technol.* **2017**, *7*, 2079.
[38] C. K. Lim, Y. S. Lee, S. H. Choa, D. Y. Lee, L. S. Park, S. Y. Nam, *Int. J. Polym. Sci.* **2017**, *2017*, 1.
[39] Y. Ji, P. Miao, R. Zhang, Q. Li, Y. Zha, F. Dai, X. Du, B. He, S. Fu, *Polym. Compos.* **2022**, *43*, 8761.
[40] X. L. Zhou, L. K. Wang, Q. W. Liao, C. Yan, X. Li, L. Qin, in *presented at 4th Int. Conf. on Advanced Engineering and Technology (ICAET)*, Incheon, South Korea, **2017**, *317*, 012016.
[41] A. Narayanan, F. Mugele, M. H. G. Duits, *Langmuir* **2017**, *33*, 1629.
[42] X. Jing, W. Zhao, L. Lan, *J. Mater. Sci. Lett.* **2000**, *19*, 377.
[43] F. Lux, *J. Mater. Sci.* **1993**, *28*, 285.
[44] G. Di Francia, A. I. Grimaldi, E. Massera, M. L. Miglietta, T. Polichetti, presented at 23rd Eurosensors Conference, Lausanne, Switzerland, **2009**, pp. 06–09.
[45] E. Skotadis, D. Mousadakos, K. Katsabrokou, S. Stathopoulos, D. Tsoukalas, *Sens. Actuators B: Chem* **2013**, *189*, 106.